

Photoionization of very high excitation gas in the Circinus galaxy and other active galactic nuclei

Luc Binette^{1,2}, Andrew S. Wilson^{3,4}, Alex Raga⁵, and Thaisa Storchi-Bergmann²

¹ European Southern Observatory, Casilla 19001, Santiago 19, Chile (e-mail: lbinette@eso.org)

² Instituto de Física, UFRGS, Campus do Vale, CxP 15051, 91501-970 Porto Alegre, RS, Brasil

³ Astronomy Department, University of Maryland, College Park, MD 20742, USA

⁴ Space Telescope Science Institute, 3700 San Martin Drive, Baltimore, Maryland 21218, USA

⁵ Instituto de Astronomía, UNAM, Ap. 70264, 04510 México, DF, México

Received 7 January 1997 / Accepted 18 June 1997

Abstract. Recent measurements of the Circinus galaxy with ISO by Moorwood et al. (1996) have confirmed the extremely high excitation of the emission-line spectrum in this active galaxy. Moorwood et al. modelled the spectrum in terms of photoionization of gas by a hard X-ray continuum plus a UV bump near 70 eV. We present new photoionization calculations which differ markedly in geometry and in the adopted spectrum of the ionizing radiation. In our model, all the zones of high excitation coexist within the internal structure of matter-bounded clouds of 1 pc thickness with a total cross section of 165 pc². A strong UV bump is not required to explain the line ratios in this picture. Our calculations consider the effects of radiation pressure exerted by photoelectric absorption which become very important at the high ionization parameters required by the line ratios. We propose that the radiation pressure generates a strong density gradient within the photoionized structure and is responsible for accelerating the matter-bounded gas, explaining the systematic blueshift observed for the coronal lines.

Key words: galaxies: active – galaxies: Seyfert – line: formation – galaxies: ISM – galaxies: Circinus galaxy

1. Introduction

Studies of the emission lines in Seyfert galaxies have indicated the presence of two different regions (cf Osterbrock 1989): a region of very high density with large velocity spread – the broad line region (BLR), and a region of low gas density and with a much smaller velocity spread – the narrow line region (NLR). There is also a set of lines of extremely high excitation, the so-called ‘coronal’ lines which includes [Fe VII] λ 6086 [Fe X] λ 6374 [Si VI]1.963 μ m and [Si VII]2.483 μ m. Korista &

Ferland (1989) showed that photoionization of a ‘warm’ interstellar gas phase could easily account for both the luminosities and the ratios of the coronal iron lines in NGC 4151. Oliva et al. (1994; hereafter OSMM) measured an extensive set of optical and infrared coronal lines in the Circinus Galaxy and showed that the line ratios could be explained better with photoionization than collisional ionization, even when a wide distribution of coronal temperatures was included in the collisional ionization model. Coronal lines are known to be systematically blueshifted (Penston et al. 1984) relative to the systemic velocity in Seyfert galaxies (by 35 km s⁻¹ in the case of Circinus, see OSMM), a property which has not been incorporated in any of the models so far.

Korista & Ferland (1989) considered the coronal gas to be of very low density (~ 1 cm⁻³) and to extend up to 2 kpc, much beyond the classical NLR but overlapping the ENLR. From the [Fe XI] line surface brightness and spatial distribution in the Circinus nucleus, OSMM derived a higher density (~ 250 cm⁻³) and a much smaller size of $\simeq 10$ pc. Both studies considered that the filling factor of the coronal gas approaches unity and that the gas density is lower than that of the NLR gas. The arguments presented, however, were partly based on the absolute ionising source luminosity, a poorly known quantity at best¹. Furthermore, this view is contradicted in the case of Circinus by the much higher density of $\sim 5\,000$ cm⁻³ inferred by Moorwood et al. (1996; Mo96) from the density sensitive [Ne V] 24.3 μ m/14.3 μ m ratio. We propose in this paper that the coronal lines do *not* originate from a pervading thin medium but from individual gas clouds, as for the NLR. In a previous paper (Binette, Wilson & Storchi-Bergmann 1996, hereafter Paper I), it was proposed that the high excitation lines originated from matter-bounded clouds. In this paper, we argue that the coronal lines originate from a subset of such matter-bounded (MB) clouds which are exposed to a much stronger continuum.

¹ For instance, Circinus has a hidden UV source while NGC4151 presents a photon deficit problem (Robinson et al. 1994).

We show in Sect. 2 that radiation pressure can no longer be neglected at the high ionization parameters implied by the coronal lines. We improve on the customary constant gas pressure model by developing a density prescription in the one-dimensional hydrostatic case which considers the distributed force represented by radiative pressure (cf. Appendix A). An interesting property of the resulting density stratification is that the gaseous excitation at high values of the ionization parameter become insensitive to further increase in the intensity of the ionizing radiation. In Sect. 3, we infer the values of the model parameters using available information on the Circinus Galaxy. In Sect. 4 we compare our model results with those of Mo96, while Sect. 5 discusses the implications of the properties of the coronal lines on the ionization-bounded and matter-bounded cloud models of Paper I.

2. The model

2.1. The computer code

The multipurpose code MAPPINGS IC was used to compute the photoionization models. As noted in Ferruit et al. (1997), the new version IC maintained by one of us (LB) now includes Fe and allows calculations of all ionization stages up to bare nuclei. The atomic data is taken from a compilation of Ralph Sutherland (see Appendix in Ferruit et al. 1997). The uncertainties in collision strengths of many coronal lines are often large (see review by Oliva 1997) and may dominate the errors in the predicted line strengths.

2.2. Two powerlaws to represent the EUV and the X-ray domains

Given the success of Paper I in accounting for a broad range of line excitation with a simple power-law with index $\gamma = -1.3$ ($\varphi_\nu \propto \nu^{+\gamma}$), we adopt a similar energy distribution. We recall that our choice of γ was motivated by the desire to produce matter-bounded (MB) clouds with high enough temperature (T_{OIII}), as indicated by the ratio $[\text{O III}]\lambda 4363/[\text{O III}]\lambda 5007$ but with the index close to the canonical values proposed in the literature (i.e., $\gamma = -1.4$ or -1.5 ; e.g., Ferland & Osterbrock 1986). The energy distribution starts at 0.1 eV. Above 500 eV we introduce a flatter component with canonical index $\gamma_X = -0.7$. We impose a high energy cut-off to this X-ray component at 100 keV (see Mathews & Ferland 1987). The resultant ionizing energy distribution is shown in Fig. 1 (dash line). It is different from that adopted by Mo96. In particular, it does not contain the pronounced UV bump at 70 eV (in a plot of $\nu\varphi_\nu$ versus ν) invoked by Mo96. By joining the UV and X-ray power-laws at 4000 eV instead of 500 eV (so as to produce a smaller $\alpha_{\text{OX}} \lesssim -1.3$), we have verified that a weaker X-ray component produces very similar results.

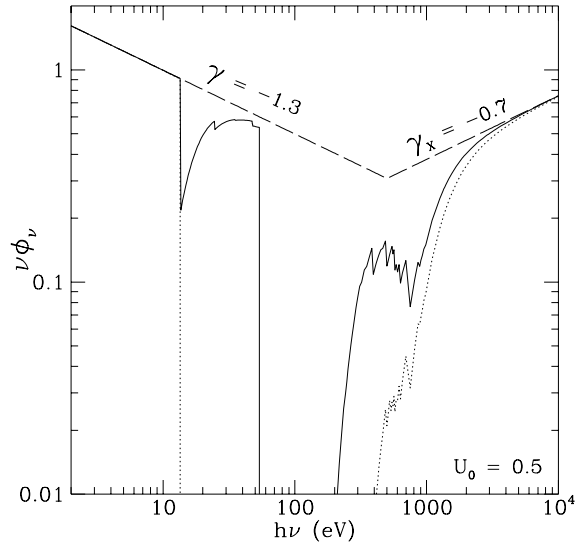


Fig. 1. Ionizing energy distributions, plotted as $\nu\varphi_\nu$ versus ν . The X-ray cut-off is at 100 keV. The long dashed line represents the direct nuclear source radiation impinging on the MB component. The solid line represents the spectrum escaping from the back of the MB slab (which contains 65% of the original number of ionizing photons). This radiation (after further geometrical dilution) impinges on the IB component. The dotted line represents the ionizing distribution escaping the back of the IB slab (only 0.9% of the number of ionizing photons but 60% of the ionizing energy flux). The energy between $\simeq 2$ keV and the cut-off at 100 keV escapes the IB slab unabsorbed.

2.3. Gas pressure vs radiation pressure

The ionization parameter U_0 is customarily defined as the ratio between the density of impinging ionizing photons and the gas density at the face of the cloud:

$$U_0 = \frac{\int_{\nu_1}^{\infty} \varphi_\nu d\nu / h\nu}{c n_0} = \frac{q_0}{c n_0} \quad (1)$$

where φ_ν is the monochromatic energy flux impinging on the cloud, ν_1 the Lyman frequency, q_0 the number of ionizing photons incident on the slab per cm^2 per second, c the speed of light and n_0 the total gas density at the irradiated surface of the slab (all quantities relevant to the irradiated surface carry 0 as a superscript or subscript).

A different definition of the ionization parameter is the following (Krolik et al. 1981) :

$$\Xi_0 = \frac{\int_{\nu_1}^{\infty} \varphi_\nu d\nu}{n_0 k T_0 c} = \frac{F_{\text{ion}}}{n_0 k T_0 c} \approx 2.3 \frac{P_{\text{rad}}}{P_{\text{gas}}^0} \quad (2)$$

where T_0 is the temperature at the irradiated surface, F_{ion} is the incident flux of ionizing radiation and k is Boltzmann's constant. Since F_{ion}/c is the pressure of the ionizing radiation (assuming the radiation is confined to a small solid angle and is normally incident on the cloud), $\Xi_0/2.3$ gives us the ratio of the pressure of ionizing radiation to the gas pressure at the irradiated face : $P_{\text{rad}}/P_{\text{gas}}^0$ (cf. Krolik et al. 1981). Radiation pressure exerts a force only if the ionizing radiation is absorbed. Even in the case

of an ionization-bounded slab, which would absorb, say, 99% of the *number* of ionizing photons (see dotted line in Fig. 1), of order 60% of the ionizing *flux* (i.e. that between ≈ 3 keV and the cut-off at 100 keV) escapes unabsorbed and therefore does not exert any force on the gas. For the matter-bounded slab discussed below, as much as 75% of the ionizing flux will not be absorbed. Therefore the actual radiation pressure absorbed by the matter-bounded slab is reduced to $P_{rad}^{abs}/P_{gas}^0 \approx 0.1 \Xi_0$. This implies that for $\Xi_0 > 10$ radiation pressure exceeds gas pressure. To determine the corresponding value of U_0 , we plot in Fig. 2 the temperature of a thin gas layer photoionized by the distribution described in Sect. 2.2 (Fig. 1, dashed line) as a function of both ionization parameters – Ξ_0 (solid line, to be read along the top axis) and U_0 (dotted line, to be read along the bottom axis). We see that U_0 is 0.25 when Ξ_0 is 10. In Sect. 2.5 we propose a density prescription in which the strong force exerted by radiation sets up an internal density gradient. The suggestion that clouds might be compressed by radiation pressure at high U was first made by Davidson (1972).

Because it corresponds to an integral of $\varphi_\nu/h\nu$, the detailed shape of the U_0 curve up to $U_0 \sim 3$ is quite insensitive to the high energy cut-off and is therefore more appropriate for determining the point where radiation pressure exceeds gas pressure (i.e. at $U_0 \geq 0.25$ for the matter-bounded slab). At the highest end of U_0 and Ξ_0 in Fig. 2, both curves join at the corresponding Compton temperature which is, however, a strong function of the X-ray cut-off. The sharp structure seen in the Ξ_0 curve around $T_0 = 10^{5.3}$ was not found in earlier work (e.g. Krolik et al. 1981; Mathews & Ferland 1987). A similar feature is nevertheless present in the more recent papers of Komossa & Fink (1997a,b) who used the code Cloudy.

2.4. Matter-bounded vs ionization-bounded clouds

The excitation mechanism of the NLR and the ENLR is generally agreed to be photoionization. However, despite broad success in fitting the strongest optical lines, there are still significant problems with photoionization models. For instance, one has the temperature problem, in which the temperature sensitive ratio $[\text{O III}]\lambda 4363/[\text{O III}]\lambda 5007$ is predicted to be smaller than is observed (Tadhunter et al. 1989; Paper I; Wilson, Binette & Storchi-Bergmann 1997). Another significant problem is that of the high excitation lines which are predicted to be much weaker than observed (e.g. $[\text{Ne V}]/\text{H}\beta$) (cf. Stasińska 1984; Viegas & Gruenwald 1988; Paper I). Shock excitation or a mixture of shock and photoionization have been proposed to resolve these discrepancies (cf., Contini & Viegas-Aldrovandi 1989, Dopita & Sutherland 1996).

In Paper I, we have shown how inclusion of photoionized matter-bounded (MB) clouds of sufficiently high excitation ($U_0=0.04$) to reproduce the high excitation $[\text{Ne V}]\lambda 3426$ lines can solve the above problems. These MB clouds were considered to be sufficiently thick to reprocess $\sim 40\%$ of the ionizing photons to which they were exposed. The low excitation lines were accounted for by a population of low ionization parameter, ionization-bounded (IB) clouds exposed to the ionizing radia-

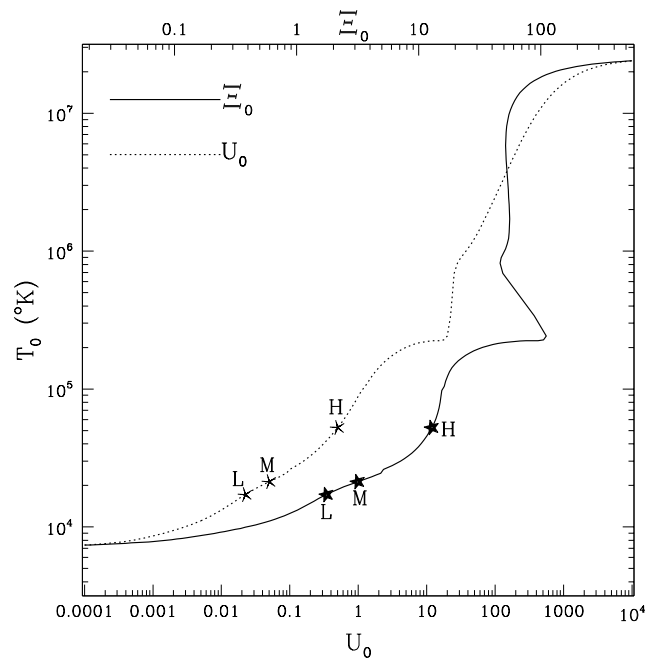


Fig. 2. Equilibrium gas temperature as a function of the pressure ionization parameter Ξ_0 (solid line, top axis) and as a function of the number density ionization parameter U_0 (dotted line, bottom axis). The position of the three models (L, M, H) of Table 1 which have $U_0 = 0.02$, 0.05 and 0.5, respectively, appear as stars on both curves.

tion spectrum which exits the MB clouds (solid line, Fig. 1). Varying the relative proportion of the two types of clouds was found to have a similar effect on the combined emission line spectrum to varying U_0 in a traditional ionization parameter sequence. We adopt here a similar scheme by considering that all the coronal lines are produced within MB clouds, some of which must evidently be much more highly excited than the clouds invoked in Paper I. The extensive set of coronal lines measured by Mo96 will be used as constraints on the physical parameters of the matter-bounded photoionized gas. The IB clouds, which account for the low excitation lines, will be discussed later in Sect. 5.

2.5. Strong density gradient as a result of radiation pressure

Binette & Raga (1989) computed the emission-line spectra emanating from one-dimensional clouds with fixed internal density gradients of arbitrary steepness. They showed that the $\beta = 1$ case (density *decreasing* outward from the center of the cloud as $x^{-\beta}$) was particularly interesting since the overall excitation of the spectrum (i.e. the emissivity averaged \bar{U}) and the line ratios tended asymptotically towards constant values, independent of the strength of the ionization radiation. This surprising result originates from the fact that a model with $\beta = 1$ generates a ‘frozen-in’ excitation structure provided U_0 is sufficiently large. Further increases in q_0 produce over-ionized zones with low emissivity at the face of the cloud; such zones do not contribute to the lines of interest. Although they did not explore how

such gradients might come about, we propose here that they result from radiation pressure. In effect, for $U_0 \gg 0.1$, the radiative force is strong enough to set up a density gradient within the cloud, which approaches the case $\beta = 1$ as demonstrated in Appendix.

Sect. A.3 in Appendix describes our implementation of the effects of radiation pressure in MAPPINGS IC. Fig. 3 shows the results of calculations with this code which confirm the asymptotic behaviour of the line ratios by comparing successive calculations with increasing ionizing photon number, q_0 (n_0 being kept constant). For instance, the [O III] $\lambda 5007$, [Ne VI] $7.66 \mu\text{m}$ and all the C, Si lines tend at very large U_0 towards constant values relative to $H\beta$. The notable exceptions are, of course, lines with low critical densities which are progressively suppressed as the increasing radiation compresses further the slab, pushing the relevant ionized zones deeper into the cloud and causing \bar{n} to increase with increasing U_0 . Alternatively, if we generate a sequence of models in which the increase in U_0 is obtained by progressively reducing the density n_0 (with q_0 held constant), as shown in Fig. 4, then the mean density \bar{n} (dotted line) as well as all line ratios tend towards a constant value at very large U_0 . In both figures, the mean ionization parameter $\bar{U} = U_0(n_0/\bar{n})$, as defined in the Appendix (Sect. A.2), tends toward a constant value.

The behaviour of the average density \bar{n} as one increases q_0 in Fig. 3b illustrates the magnitude of the density gradient across the MB structure : first, there is a gradual increase of \bar{n} with increasing U_0 (for $U_0 < 0.1$) then a more rapid change (for $U_0 > 0.1$). When \bar{n} and U_0 become proportional, \bar{U} is constant (see eqs. A.12–A.14) indicating that the excitation structure relative to the Strömgen boundary is ‘frozen in’. In Fig. 3a and 4a, the short dash line describes the relative importance of the radiation pressure absorbed within the MB slab, which exceeds P_{gas}^0 for $U_0 > 0.2$.

3. Model parameters inferred from Circinus

3.1. A high ionization parameter

The strengths of the extremely high excitation lines, such as [S IX] and [Si IX], observed by OSMM in the Circinus Galaxy could not be reproduced using the ionization parameter $U_0 = 0.04$ adopted in Paper I. As a first step, we determined that values as high as $U_0 = 0.5$ are needed to account for the relative strength of [S IX] $1.25 \mu\text{m}$ and [Si IX] $3.935 \mu\text{m}$. Adopting $U_0 = 0.5$, the second step consisted of determining the thickness of the high excitation MB clouds. This was obtained by simply requiring that the model fit the relative strengths of all three infrared silicon lines. These span a wide range in excitation yet are exclusively produced within the MB component. In our calculations, [Si VI] effectively sets the thickness of the MB slab since too much [Si VI] is generated if the MB component is excessively thick. In short, the Si species observed in the ratio: $\{[\text{Si VI}] 1.963 \mu\text{m} : [\text{Si VII}] 2.483 \mu\text{m} : [\text{Si IX}] 3.935 \mu\text{m}\} = \{0.60 : 1.0 : 1.3\}$ were successfully reproduced with a slab thickness such that 35% of

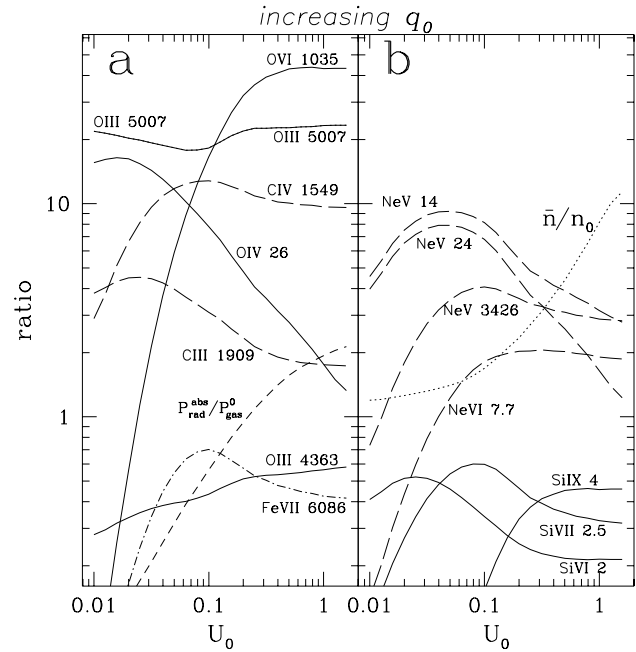


Fig. 3a and b. High excitation line ratios relative to $H\beta$ emitted by a matter-bounded slab which reprocesses 35% of the incident ionizing radiation. The calculations were performed for a range of ionization parameter (U_0) obtained by increasing q_0 and taking into account the variation of density with distance into the cloud resulting from radiation pressure (Sect. 2.5). The lines are labelled with their wavelength in Å or μm . **a** oxygen (solid line), iron (dotted-dashed line) and carbon (long dash line). The short dash line indicates the relative importance of the radiative pressure exerted within the MB slab. **b** neon (long dash line) and silicon (solid line). The dotted line represents the average density relative to the density $n_0 (= 1000 \text{ cm}^{-3})$ at the irradiated surface of the slab. For $U_0 \gg 0.1$, line ratios of density stratified models tend asymptotically towards constant values except for the density sensitive lines like [O IV] $25.90 \mu\text{m}$, [Ne V] $24.31 \mu\text{m}$ and [Ne V] $14.32 \mu\text{m}$.

the ionizing photons are absorbed by the MB slab. This number is very similar to that favored in Paper I.

3.2. The density

To select the density, we also proceed from observations. As indicated by Mo96, the [Ne V] $24.3 \mu\text{m}/14.3 \mu\text{m}$ line ratio provides an excellent density diagnostic for the high excitation gas. The observed value of 1.5 indicates a density $\approx 5000 \text{ cm}^{-3}$ for the [Ne V] emitting gas. This ratio is reproduced in our model with $U_0 = 0.5$ by adopting a density at the irradiated cloud surface of $n_0 = 1000 \text{ cm}^{-3}$. As a result of the increasing density with increasing distance into the MB slab, reaching 12000 cm^{-3} at the back of the cloud, the [Ne V] emitting region has the appropriate average density of $\approx 4700 \text{ cm}^{-3}$.

3.3. Solar metallicity and dust-free gas

We assume the gas is dust-free and of solar metallicity (Anders & Grevesse 1989). An absence of dust in the MB cloud can be

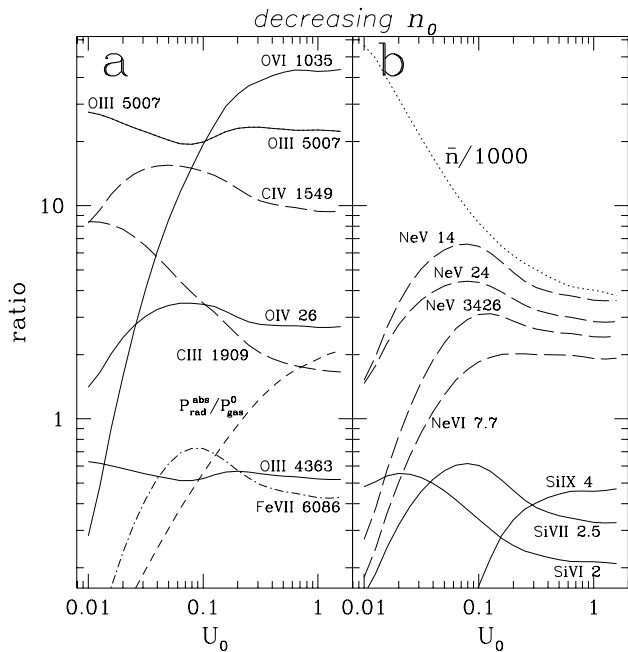


Fig. 4a and b. Same as in Fig. 3 except that the increase in U_0 was obtained by decreasing n_0 . For $U_0 \gg 0.1$, the mean density $\bar{n}/1000 \text{ cm}^{-3}$ and all line ratios tend asymptotically towards a constant value.

justified on the grounds that the strength of $[\text{Ca VIII}]2.321 \mu\text{m}$ is perfectly consistent with the solar Ca/H abundance ratio, therefore implying that depletion into dust grains is negligible (see OSMM). It is worth noting that OSMM did not detect any $[\text{Ca II}]\lambda 7291$ while its strength is predicted to exceed observed neighboring lines of $[\text{Ar III}]\lambda 7135$ and $[\text{O II}]\lambda 7325$ (cf. Table 1). This suggests that dust is probably present in the low excitation IB component (Villar-Martín & Binette 1996).

3.4. Line ratios from the high excitation MB cloud

As described in the above subsections, we adopt $U_0=0.5$, and $n_0=1000 \text{ cm}^{-3}$ for our MB cloud which absorbs $\simeq 35\%$ of the incident ionizing radiation. The calculated UV, optical and infrared line strengths are presented in Table 1 and are identified as model H (third column, heading R_{MB}^i). For comparison, we include in Table 1 two other models, M and L, which differ only in their lower ionization parameters of $U_0 = 0.05$ and 0.02 , respectively. The discussion of these and of their corresponding low excitation IB components (heading R_{IB}^i in Table 1) is postponed to Sect. 5.

4. Results and comparison with Circinus

4.1. Comparison with coronal line ratios

OSMM observed lines of very high excitation, mostly found in the infrared, in the Circinus Galaxy. Mo96 recently augmented the dataset with ISO observations out to $45 \mu\text{m}$.

We now compare the spectrum of model H (Table 1) with the coronal lines observed in Circinus. As the $[\text{Si IX}]\lambda 3.935 \mu\text{m}$

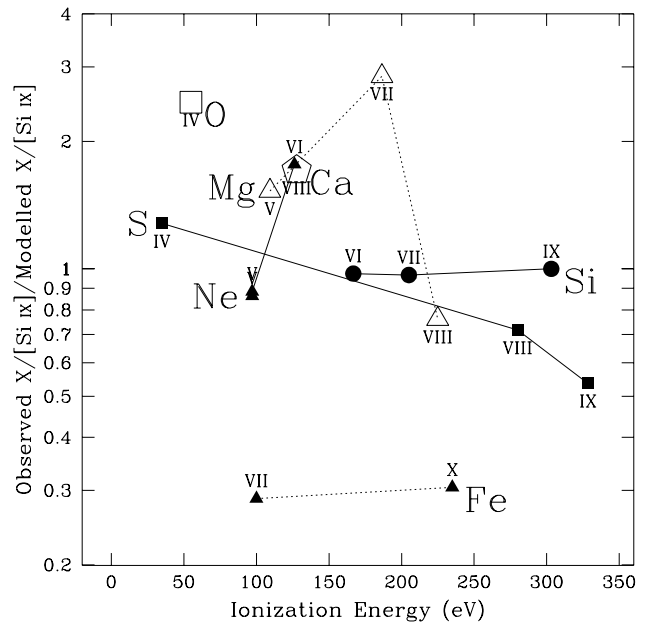


Fig. 5. Observed divided by modelled line flux ratios, where all ratios are expressed relative to $[\text{Si IX}]\lambda 3.935 \mu\text{m}$. The lines plotted include $[\text{O IV}]\lambda 25.90 \mu\text{m}$ (open square), $[\text{Si VI}]\lambda 1.963 \mu\text{m}$, $[\text{Si VII}]\lambda 2.483 \mu\text{m}$, $[\text{Si IX}]\lambda 3.935 \mu\text{m}$ (filled circles), $[\text{S IV}]\lambda 10.54 \mu\text{m}$, $[\text{S VIII}]\lambda 9913$, $[\text{S IX}]\lambda 1.25 \mu\text{m}$ (filled squares), $[\text{Ne V}]\lambda 14.32 \mu\text{m}$, $[\text{Ne V}]\lambda 24.31 \mu\text{m}$, $[\text{Ne VI}]\lambda 7.66 \mu\text{m}$ (upper filled triangles), $[\text{Mg V}]\lambda 5.62 \mu\text{m}$, $[\text{Mg VII}]\lambda 5.51 \mu\text{m}$, $[\text{Mg VIII}]\lambda 3.03 \mu\text{m}$ (open triangles), $[\text{Ca VIII}]\lambda 2.321 \mu\text{m}$ (open pentagon), $[\text{Fe VII}]\lambda 6086$ and $[\text{Fe X}]\lambda 6374$ (lower filled triangles). The model is a stratified matter-bounded slab with $U_0=0.5$.

line was measured both by ISO (Mo96) and from the ground (OSMM), we combined the two data sets by expressing all line ratios relative to their respective $[\text{Si IX}]$ flux measurement. As a rule, we retain the OSMM ratios only for the lines not measured with ISO (e.g. $[\text{Fe X}]\lambda 6374$). Note that the optical groundbased observations were corrected for reddening ($A_V = 5.2$) while the ISO data was not. Reddening is of little consequence in the mid- and far-infrared since the correction is smaller than the observational errors.

We present in Fig. 5 the ratio of observed to model line fluxes as a function of ionization energy. This diagram may be compared directly with the corresponding Fig. 4 of Mo96. We have omitted $[\text{Ne III}]\lambda 15.55 \mu\text{m}$ since this line is dominated by the IB component (cf. Table 1). The degree of agreement between model and observations is similar for our model and that of Mo96. Except for the iron lines (discussed below, but not shown in Fig. 4 of Mo96) and $[\text{Mg VII}]\lambda 5.51 \mu\text{m}$, the dispersion in our Fig. 5 is less than a factor of two, which represents good agreement considering the uncertainties in atomic data (see review by Oliva 1997). The discrepancy between our results and those of Mo96 for $[\text{Mg VII}]\lambda 5.51 \mu\text{m}$ is probably due to the use of different atomic data. We therefore conclude that MB clouds with internal density gradients induced by radiation pressure are equally successful in fitting the observations as the onion ring geometry with a UV bump studied by OSMM and Mo96.

Table 1. MB and IB line ratios relative to $H\beta$ (=1.00)

	Label	Model H		Model M		Model L	
	U_0	0.5		0.05		0.02	
	$C_{M/I}$	0.461		0.368		0.354	
Species	λ	R_{MB}^i	R_{IB}^i	R_{MB}^i	R_{IB}^i	R_{MB}^i	R_{IB}^i
H α	6563 Å	2.76	2.89	2.77	2.93	2.79	2.95
He II	1640 Å	5.14	$5.6 \cdot 10^{-3}$	6.52	$8.6 \cdot 10^{-3}$	5.78	$1.08 \cdot 10^{-2}$
He II	4686 Å	0.60	$1.0 \cdot 10^{-3}$	0.85	$1.6 \cdot 10^{-3}$	0.84	$2.0 \cdot 10^{-3}$
He I	5876 Å	$4.8 \cdot 10^{-2}$	0.16	$2.8 \cdot 10^{-2}$	0.19	$3.5 \cdot 10^{-2}$	0.20
C IV	1549 ^b Å	9.95	$5.3 \cdot 10^{-4}$	11.9	0	6.58	0
C III]	1909 ^b Å	1.83	0.39	4.00	0.10	4.50	$4.5 \cdot 10^{-2}$
C II]	2326 Å	0	0.12	0	0.14	$2.2 \cdot 10^{-4}$	0.11
N V	1240 ^b Å	4.0	0	2.01	0	0.47	0
N III]	1749 ^b Å	0.15	$7.4 \cdot 10^{-3}$	0.28	$3.9 \cdot 10^{-4}$	0.29	0
[N II]	5755 Å	$9.3 \cdot 10^{-5}$	$5.00 \cdot 10^{-2}$	$3.6 \cdot 10^{-4}$	$3.54 \cdot 10^{-2}$	$1.1 \cdot 10^{-3}$	$2.72 \cdot 10^{-2}$
[N II]	6583 Å	$2.5 \cdot 10^{-3}$	3.46	$9.1 \cdot 10^{-3}$	3.20	$3.4 \cdot 10^{-2}$	2.78
[N I]	5200 ^b Å	0	0.31	0	0.23	0	0.25
O VI	1035 ^b Å	42.6	$2.0 \cdot 10^{-4}$	5.66	0	0.48	0
O V]	1218 Å	9.04	0	3.63	0	0.74	0
[O IV]	25.9 μ m	2.74	$8.1 \cdot 10^{-4}$	11.7	$1.4 \cdot 10^{-4}$	16.3	0
O III]	1663 ^b Å	1.61	$1.4 \cdot 10^{-2}$	1.02	$6.6 \cdot 10^{-4}$	0.72	$1.2 \cdot 10^{-4}$
[O III]	4363 Å	0.538	$1.63 \cdot 10^{-2}$	0.393	$8.75 \cdot 10^{-4}$	0.336	$1.70 \cdot 10^{-4}$
[O III]	5007 Å	22.8	3.56	18.2	0.24	20.3	$5.2 \cdot 10^{-2}$
[O II]	3727 ^b Å	$2.7 \cdot 10^{-2}$	5.48	$8.3 \cdot 10^{-2}$	5.19	0.20	4.10
[O II]	7330 ^b Å	$2.6 \cdot 10^{-3}$	0.20	$3.0 \cdot 10^{-3}$	$8.9 \cdot 10^{-2}$	$5.5 \cdot 10^{-3}$	$5.6 \cdot 10^{-2}$
[O I]	6300 Å	0	1.15	0	0.97	0	1.0
[Ne VI]	7.6 μ m	2.01	0	1.23	0	0.42	0
[Ne V]	3426 Å	3.05	0	3.58	0	1.78	0
[Ne V]	14.3 μ m	3.86	$2.7 \cdot 10^{-4}$	9.32	0	7.54	0
[Ne V]	24.2 μ m	2.55	$1.3 \cdot 10^{-4}$	8.02	0	6.56	0
[Ne IV]	2423 ^b Å	1.12	0	1.84	0	1.58	0
[Ne III]	3869 Å	1.37	0.66	0.98	0.20	1.19	$8.4 \cdot 10^{-2}$
[Ne III]	15.6 μ m	0.84	1.61	0.56	0.66	0.84	0.33
[Ne II]	12.8 μ m	$9.7 \cdot 10^{-4}$	3.42	$9.8 \cdot 10^{-4}$	2.18	$2.5 \cdot 10^{-3}$	1.74
[Mg VIII]	3.3 μ m	0.77	0	0.27	0	$4.3 \cdot 10^{-2}$	0
[Mg VII]	5.5 μ m	0.19	0	0.26	0	0.10	0
[Mg V]	5.6 μ m	0.29	0	0.47	0	0.81	0
Mg II	2800 Å	$4.49 \cdot 10^{-3}$	2.61	$3.1 \cdot 10^{-3}$	1.92	$1.1 \cdot 10^{-2}$	1.63
[Si IX]	3.93 μ m	0.45	0	$3.9 \cdot 10^{-2}$	0	$2.8 \cdot 10^{-3}$	0
[Si VII]	2.48 μ m	0.35	0	0.54	0	0.27	0
[Si VI]	1.96 μ m	0.22	0	0.46	0	0.52	0
[S IX]	1.25 μ m	0.18	0	$1.4 \cdot 10^{-2}$	0	$4.2 \cdot 10^{-4}$	0
[S VIII]	9913 Å	0.14	0	$5.4 \cdot 10^{-2}$	0	$4.4 \cdot 10^{-3}$	0
[S IV]	10.5 μ m	0.99	$5.0 \cdot 10^{-2}$	1.37	$3.5 \cdot 10^{-3}$	2.41	$1.02 \cdot 10^{-3}$
[S III]	9531 Å	$3.9 \cdot 10^{-2}$	2.56	$5.6 \cdot 10^{-2}$	1.48	0.15	1.06
[S III]	18.7 μ m	$7.5 \cdot 10^{-3}$	1.33	$1.7 \cdot 10^{-2}$	1.08	$4.9 \cdot 10^{-2}$	0.80
[S III]	33.6 μ m	$1.6 \cdot 10^{-3}$	0.64	$9.5 \cdot 10^{-3}$	0.95	$3.2 \cdot 10^{-2}$	0.82
[S II]	4072 ^b Å	0	0.27	0	0.22	0	0.22
[S II]	6716 Å	0	1.25	$1.2 \cdot 10^{-4}$	1.12	$5.4 \cdot 10^{-4}$	1.23
[S II]	6731 Å	0	1.67	$1.6 \cdot 10^{-4}$	1.41	$7.0 \cdot 10^{-4}$	1.53
[Ca VIII]	2.32 ^a μ m	$9.2 \cdot 10^{-2}$	0	$2.5 \cdot 10^{-2}$	0	$2.7 \cdot 10^{-3}$	0
[Ca II]	7291 ^a Å	$4.7 \cdot 10^{-4}$	1.24	$1.3 \cdot 10^{-3}$	1.51	$7.4 \cdot 10^{-3}$	1.46
[Fe X]	6374 Å	0.81	0	$1.5 \cdot 10^{-2}$	0	$2.4 \cdot 10^{-4}$	0
[Fe VII]	6086 Å	0.46	0	0.55	0	0.16	0

^a Ca/H is *not* depleted^b Sum of doublet terms

4.2. ‘Onion’ ring vs cloud geometry

As in Korista & Ferland (1989), OSMM considered that the high excitation gas in Circinus has a filling factor close to unity and a geometry analogous to that of a multilayered ‘onion’, with the excitation of the gas decreasing radially as a result of the increasing dilution of the nuclear radiation. We have proposed here a different geometry in which each individual cloud is sufficiently stratified in excitation to emit the entire observed range of high excitation lines. In our model, the basic difference between NLR clouds and the gas emitting the coronal lines is that the latter have a much higher ionization parameter. On the other hand, the alternative ‘onion’ ring geometry presupposes a uniform distribution of gas which differs from the very low volume filling factor believed to characterize the NLR (Osterbrock 1989). In the specific case of Circinus, a uniform spherical distribution of coronal gas at the high density inferred from the $[\text{Ne V}] 24.3 \mu\text{m}/14.3 \mu\text{m}$ ratio implies that the highest excitation species are confined to radii smaller than $0.2''$ (Mo96); otherwise the coronal line luminosities would exceed the observed level². To the extent that the photon luminosity of the source is unconstrained, this limit in radial distance does not apply to our model since our line luminosities are governed by the covering factor, which is a free parameter.

The geometrical depth of our internally stratified cloud in model H is only 1 pc (hydrogen column density of 7.8×10^{21} atoms cm^{-2}), or $\simeq 0.05''$ at the distance of Circinus ($D = 4$ Mpc). Knowing \bar{n} of the coronal gas, the brightness predicted for $[\text{Si IX}]3.935 \mu\text{m}$ by model H, and the observed $[\text{Si IX}]3.935 \mu\text{m}$ luminosity in Circinus ($\simeq 6.1 \cdot 10^{-13}$ erg $\text{cm}^{-2} \text{s}^{-1}$ after correcting for extinction), we infer that the total cross sectional area of the MB clouds responsible for the coronal line emission must be $165(D/4 \text{ Mpc})^2 \text{pc}^2$. This would imply a covering factor Ω_{MB} of 0.13 if the clouds were to lie at a mean radius of 10 pc ($0.5''$) from an isotropic nuclear source. The inferred ionizing photon luminosity in this case is $10^{52.4}/\Omega_{\text{MB}}$ for an isotropic source, which is similar to the value derived by Mo96.

4.3. The iron lines

Although encouraging, Fig. 5 shows significant discrepancies in the case of the optical Fe lines (which were left out of Fig. 4 of Mo96). One possible explanation is the large uncertainty in the collision strengths of some Fe transitions. Chief among these is $[\text{Fe X}]\lambda 6374$ for which recent determinations of the collision strength by Mohan et al. (1994) and Pelan & Berrington (1995) differ by an order of magnitude. Another factor is the large extinction. If obscuration is nonuniform over the nuclear regions of the Circinus Galaxy, dereddening of the emission line spectrum is not possible without precise knowledge of the dust distribution. The fact that the Fe lines are the only *optical* lines in Fig. 5 is probably not a coincidence. It is conceivable that one sees in the optical only a small portion of the emission region

² A very thin isobaric shell of large radius is not allowed either since its ionization structure would not encompass a sufficiently wide range in excitation.

observed in the far infrared. Finally, model H cannot account for the luminosity of $[\text{Fe XI}]\lambda 7892$ as observed by OSMM.

4.4. The energy distribution: UV bump or no UV bump?

Since our fit to the line ratios is of similar quality to that of Mo96, we argue that one cannot uniquely determine the spectrum of the ionizing radiation from the emission-line ratios. We do not exclude the possibility of a UV bump but consider that its existence cannot be proven with the line ratios plotted in Fig. 5. We have explored using various energy distributions, some very similar to that of Mo96, but without obtaining any real improvement. The most likely explanation for this difference between our results and those of Mo96 is the presence of density gradients in our models. Internally stratified slabs produce a significantly ‘richer’ mixture of high and low excitation lines in comparison with the standard isobaric models (Binette & Raga 1990). Even if we lower the X-ray luminosity by joining the two power-laws of Fig. 1 (dash-lines) at 4 000 eV instead of 500 eV, we obtain almost indistinguishable results by simply using a slightly lower U_0 .

5. The intermediate and low excitation lines

5.1. Rarity of clouds with coronal line emission

OSMM showed that unlike the coronal lines, the velocities of the optical lines of $[\text{O III}]\lambda 5007$, $[\text{N II}]\lambda 6583$, $[\text{O I}]$, $[\text{S II}]$, $\text{H}\beta$ and $\text{He II} \lambda 4686$ are essentially consistent with systemic. Inspired by the work of Viegas & Prieto (1992), we have discussed in Paper I the possible existence of two populations of clouds to explain the range of gaseous excitation observed in the optical in a small sample of Seyfert and radio galaxies. What are the implications of a much higher excitation component for this kind of model? Although the matter-bounded component of model H does account for the coronal lines, it is probably unsuitable for the bulk of the intermediate excitation lines (e.g. $[\text{O III}]$), which are at least in part kinematically distinct (OSMM). There must also be gas of lower excitation because the ratios of the coronal lines to the recombination lines are larger in model H than is observed. For instance, adopting a recombination case B ratio of $\text{Br}\alpha/\text{H}\beta = 0.06$ ($T_e = 20\,000$ K), we infer that the $[\text{Si IX}]3.935 \mu\text{m}/\text{H}\beta$ ratio in Circinus is ≈ 0.066 . This value is 7 times smaller than that predicted by the matter-bounded component of model H. Of course part or all of the ionizing radiation escaping the MB slab (65%) can be reprocessed by more distant/denser low excitation clouds. However, even allowing for this (adopting $A_{\text{M/I}}=2.5$ as discussed below), we find that the coronal gas component must have a covering factor of only a quarter of that of other less excited but still matter-bounded clouds. For this reason, we have calculated MB models of lower U_0 (Table 1). As the lowest excitation coronal lines (e.g. $[\text{Si VI}]$, $[\text{O IV}]$, $[\text{S IV}]$) in Fig. 5 can be produced by the lower U_0 models, a proper fit of all the coronal lines would entail combining model H with other models of lesser excitation such as the MB component of model M ($U_0 = 0.05$). We believe, however, that such an attempt is premature given the

few constraints available and the uncertainties in atomic data and metallicity.

5.2. The low excitation IB component

Whether or not the observations require a range in excitation for the MB clouds, 65% of the impinging ionizing photons still escape those clouds. We therefore propose, as in Paper I, that some of these unabsorbed photons are absorbed at larger radii and reprocessed into the observed low excitation lines. This component, dubbed IB (ionization-bounded) in Paper I, can be calculated for each MB component in Table 1 once we decide on its ionization parameter U_{IB} . As we do not have enough information to determine the proper combination of the matter-bounded models H, M and L, we are even less inclined to try to determine which IB component is most appropriate. The IB line spectra listed in Table. 1 are therefore tentative and are intended for comparison with other Seyferts.

As U_{IB} cannot be constrained from the optical spectrum of Circinus alone, we have adopted as constraints the same sample of line ratios as in Paper I, which are representative of the ENLR of Seyfert and radio galaxies. We found that an ionization parameter of $U_{IB} = 6.5 \cdot 10^{-4}$ allows model H (see following sections) to fit reasonably well most of the line ratios covered in Paper I. This U_{IB} is realized by simply applying a geometrical dilution factor of 10^{-2} to the spectrum transmitted through the MB component. For definiteness we have set U_{IB} constant for all three models. For some of the lines, the intensities are quite similar across the three IB models of Table 1 (e.g. [O II] $\lambda\lambda 3727$, [O I] $\lambda 6300$, [S II] $\lambda\lambda 6724$ and [N II] $\lambda 6583$). We have not explored a lower density IB component (of equal U_{IB} , therefore implying a higher dilution of the radiation) as would be required to account for the low density inferred from [S II] in Circinus ($\approx 400 \text{ cm}^{-3}$). Such a procedure, however, has been successfully applied by Rodriguez-Ardilla et al. (1997) to the two Seyferts A08.12 and F10.01 which are characterized by a much larger density contrast between the high and low excitation emission line regions.

5.2.1. The parametrized $A_{M/I}$ -sequence

The parameter $A_{M/I}$ is used to represent the relative proportion of visible MB and IB clouds. It is a free parameter which alters the level of excitation of the spectra in much the same way as the ionization parameter in traditional photoionization models. A sequence of models as a function of $A_{M/I}$ may be obtained by combining the MB and IB spectra of any of the three models of Table 1 as follows:

$$R_{\text{seq}}^i(A_{M/I}) = \frac{R_{IB}^i + C_{M/I} A_{M/I} R_{MB}^i}{1 + C_{M/I} A_{M/I}} \quad (3)$$

where R_{seq}^i , R_{MB}^i , R_{IB}^i are the line ratios relative to $H\beta$ of line i . $C_{M/I}$ represents the luminosity ratio of the $H\beta$ produced by the MB component relative to the IB component and is a constant for a given model.

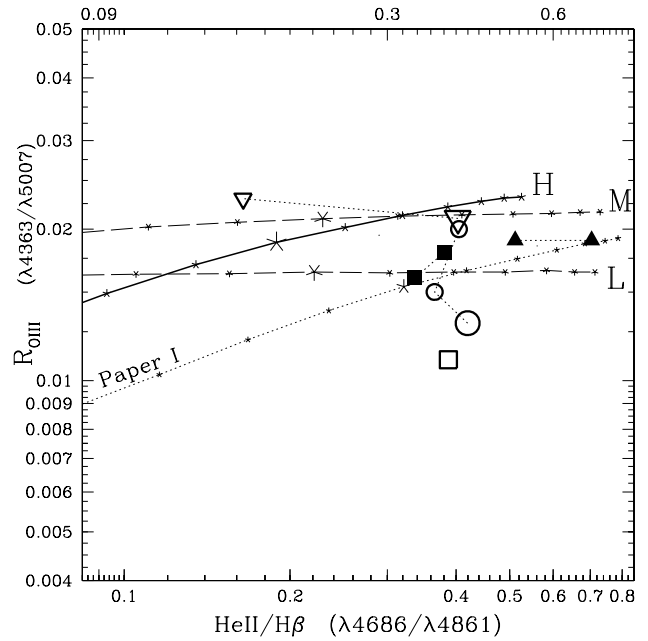


Fig. 6. Diagram of the temperature sensitive line ratio R_{OIII} ($4363\text{\AA}/5007\text{\AA}$) against $\text{He II}/\text{H}\beta$. Filled symbols represent radio galaxies while open symbols are for Seyferts. Dotted lines join measurements at different locations in the same galaxy. Smaller symbols denote extended emission line regions (EELR) while the larger symbols denote the nuclear ratios (NLR). The solid line represents the $A_{M/I}$ -sequence ($0.04 \leq A_{M/I} \leq 16$) of our model H with $A_{M/I}$ increasing from left to right along the solid line. The asterisks are separated by 0.2 dex in $A_{M/I}$ and the larger asterisk denotes the position of the model with $A_{M/I} = 1$ (see eqn. 3). The long dashed lines represent $A_{M/I}$ -sequences of models M and L. The dotted line represents the lower density $A_{M/I}$ -sequence of Paper I.

Our scheme for using matter-bounded components is fairly simple and basic as it recognizes only two populations of clouds. However, as shown in Paper 1, it presents significant advantages, including a resolution of the temperature problem. Other schemes in which a continuous range of cloud opacity is considered for the NLR or ENLR gas can be found in Komossa & Shulz (1997), Nazarova et al. (1997), Moore & Cohen (1994, 1996), Acosta et al. (1996), Morganti et al. (1991) and Binette (1984).

5.2.2. Comparison with Paper I

The $A_{M/I}$ -sequence of model H (solid line) is plotted in Figs. 6 and 7. The most direct measure of $A_{M/I}$ is the $\text{He II } \lambda 4686/\text{H}\beta$ ratio. In the Circinus Galaxy, the dereddened ratio of 0.32 of OSMM indicates a value of $A_{M/I} \sim 2.5$.

In Fig. 6 we see that model H reaches $R_{OIII} = 0.02$, corresponding to $T_e \simeq 15000 \text{ K}$ (at a density of 10^4 cm^{-3}), in agreement with the high EELR temperatures inferred by Storchi-Bergmann et al. (1996) and Wilson, Binette & Storchi-Bergmann (1997). Fig. 7 indicates that very small [N II] $\lambda 6583/\text{H}\alpha$ ratios, as observed in Pks 0349-27 (filled tri-

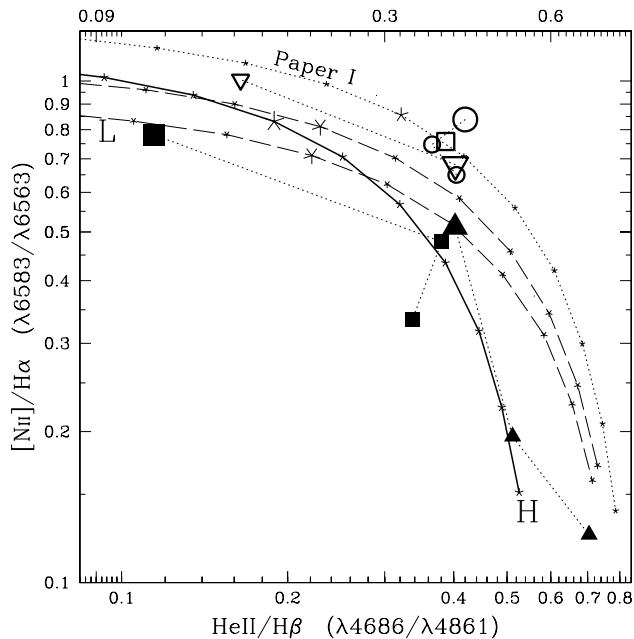


Fig. 7. Diagram of the line ratios $[N II]/H\alpha$ against $He II/H\beta$. The symbols and lines have the same meaning as in Fig. 6.

angles), are not necessarily a signature of star formation but a natural consequence of having a region dominated by matter-bounded clouds (Binette 1984).

6. Conclusions

We have studied the possibility that dense matter-bounded clouds are responsible for the emission of the coronal lines in the Circinus galaxy. In our scheme, the clouds emitting the coronal lines have a much higher ionization parameter (U_0) than those responsible for the rest of the narrow lines. Further, the high values of U_0 implied by the observed $[Si IX]/[Si VI]$ ratio implies that radiation pressure exceeds gas pressure. We have incorporated the effects of radiation pressure into our calculations and shown that strong density gradients result. The density gradient is similar to the case $n(x) \propto x^{-1}$ discussed by Binette & Raga (1990). The agreement between our density stratified MB model and the observed coronal line ratios in Circinus is very encouraging, and leads us to suspect that the blueshift characterizing the coronal gas might result from radiative acceleration.

Acknowledgements. Calculations with MAPPINGS IC were carried on the ESO *sc0* workstation. We thank the referee Hagai Netzer for the many constructive comments and Alan Moorwood for making available ISO results in advance of publication. LB is grateful to CNPq and CAPES of Brasil for financial assistance. This research was supported in part by NASA through grant NAGW 4700.

Appendix A: density gradients from radiation pressure

It is customary to assume constant pressure in photoionization calculations, i.e. to employ at each point of the nebula a total

density which depends on the local temperature and on the ionization fraction of H and He. The dynamical impact of the impinging radiation is not considered and the gas is assumed static. These assumptions can be justified by the fact that, in general, the timescales for photoionized plasmas to reach local thermal and ionization equilibrium are much shorter than the dynamical timescales. From this perspective, photoionization models represent a series of “snapshots” of the nebular ionization and density structure. However, if one adopts unusually large ionization parameters ($U > 0.1$) radiation pressure can no longer be ignored, since it exceeds gas pressure, as shown in Sect 2.3. To take account of radiation pressure in a semi-quantitative manner in the one dimensional case, we have developed a density prescription which is consistent with the assumption of hydrostatic equilibrium, but takes into account the force exerted by radiation from an external source.

If a cloud of neutral gas is suddenly irradiated by an external ionizing radiation field, the cloud surface becomes ionized, and an ionization front travels into the cloud. The photoionized layer is heated to $T \sim 10^4$ K, resulting in a substantial overpressure which drives an outward flow of gas whose density decreases (thereby increasing U) with time. However, in the one dimensional case, the radiation pressure of the photon field on the gas will tend to stop this outward flow. Let us consider what happens in one dimension if the gas density profile evolves towards that of a balance between the gas pressure gradient (directed outward) and the force due to the gradual absorption of the incident ionizing photon field (directed inward).

For the simple case of a pure hydrogen slab we derive (Sect. A.1) analytical expressions describing the principles behind the production of a density gradient by radiation pressure. In Sect. A.2, we discuss some of the properties of internal density gradients, while in Sect. A.3 we describe the numerical implementation of this density prescription in MAPPINGS IC, which includes elements other than hydrogen.

A.1. Density behaviour in the hydrostatic case

Let us assume that the line emission originates from gas clouds which are ‘near’ hydrostatic equilibrium. We assume that the emitting region consist of many clouds at various distances r_i from the central ionizing source. In this scheme, the cloud dimensions are much smaller than r_i , which allows us to approximate each cloud as a slab and to describe its characteristics in the one dimension x . Unlike other works on ionized nebulae and only for the purpose of simplifying the analytical expressions, we adopt the convention that the spatial coordinate x increases outward from the cloud interior, having its origin beyond the position of the “Strömgen boundary” x_S where hydrogen becomes neutral. Note that all quantities measured at the irradiated surface (i.e. at $x = L$, cf. equations A.10–A.11) carry 0 as a superscript or a subscript.

The clouds may or may not be of the same density. If their ‘front’ density n_i^0 (i.e. at their irradiated face) was to differ such that $n_i^0 \propto r_i^{-2}$ then the ratio of radiation pressure to gas pressure would be the same for all clouds. On the other hand,

if their ‘front’ densities were all the same, the impact on each cloud of the radiation pressure would be a decreasing function of the distance from the ionizing source.

Let us now concentrate on a single cloud which in our simplified treatment is approximated as an isothermal *pure* hydrogen ionization-bounded photoionized slab. We have the equation of state :

$$P = 2 n k T, \quad (A.1)$$

where P is the local gas pressure, n ($= n_{HII} = n_e$) the proton density (function of x) and T the temperature (a constant). Neglecting the presence of other forces, we have :

$$\frac{dP}{dx} = -F_{rad} = -n_{HI}\xi, \quad (A.2)$$

where F_{rad} is the force produced by the radiation pressure as a result of photoelectric absorption and n_{HI} ($\ll n_{HII}$) is the number density of neutral hydrogen. ξ is given by :

$$\xi = \int_{\nu_1}^{\infty} \frac{\varphi_{\nu}}{h\nu} \frac{h\nu}{c} a_{\nu} d\nu. \quad (A.3)$$

where φ_{ν} is the monochromatic ionizing energy flux impinging on the cloud and a_{ν} the photoionization cross section from the ground state of hydrogen. The equilibrium ionization balance of hydrogen is described by :

$$n_{HI} = \frac{n^2 \alpha_B}{\psi}, \quad (A.4)$$

where α_B is the hydrogen radiative recombination coefficient to excited states and ψ is given by :

$$\psi = \int_{\nu_1}^{\infty} \frac{\varphi_{\nu}}{h\nu} a_{\nu} d\nu. \quad (A.5)$$

Combining equations A.1–A.4 and assuming an *isothermal* temperature distribution, we obtain :

$$\frac{dn}{dx} = -n^2 \frac{\alpha_B \xi}{2kT \psi}. \quad (A.6)$$

A simple solution to this differential equation can be obtained if we neglect the effects of the diffuse radiation and the hardening of the ionizing photon field. In this approximation, the ratio ξ/ψ is independent of x and so is a constant in the integration of eqn. A.6. We should note that for a $\varphi_{\nu} \propto \nu^{\gamma}$ power law ionizing photon field, this ratio takes the simple form :

$$\frac{\xi}{\psi} = \frac{h\nu_1}{c} \left(\frac{3-\gamma}{2-\gamma} \right), \quad (A.7)$$

where ν_1 is the Lyman frequency, and we have made use of the fact that $a_{\nu} \propto \nu^{-3}$. In this way, we can integrate eqn. A.6 to obtain the important result that the position-dependent density of the cloud, $n(x)$, *decreases outward*, namely :

$$n(x) = \frac{n_0 L}{x}, \quad (A.8)$$

where n_0 is the density at the outer boundary ($x = L$) of the cloud. The product $n_0 L$, the significance of which is discussed below, contains the following constants :

$$n_0 L = \frac{2kT \psi}{\alpha_B \xi} = \frac{2kT}{\alpha_B} \frac{c}{h\nu_1} \left(\frac{2-\gamma}{3-\gamma} \right). \quad (A.9)$$

The implied divergence of the gas density for $x \rightarrow 0$ in eqn. A.6 is an artifact of not considering opacity explicitly in equations A.3 and A.5. As power law continua generate an extensive semi-ionized region, the details of the transition between the fully ionized region and the neutral region at $x \leq x_S$ are not described in the above simplified formulation. As described in Sect. A.3, these two limitations are overcome in MAPPINGS IC by properly solving for the transfer across the slab and by taking into account the opacity of all abundant metals and ions.

A.2. Implications of strong density stratification

In a paper by Binette & Raga (1990; BR90), photoionization calculations were presented in which the gaseous condensations had ‘built-in’ density stratification with a density profile of the form :

$$n(x) = n_0 \left(\frac{L}{x} \right)^{\beta}; x \leq L, \quad (A.10)$$

$$n(x) = 0; x > L \quad (A.11)$$

where n_0 corresponds to the density at the slab’s irradiated surface (i.e. at $x = L$). It was found that when the density decreases outward as x^{-1} (i.e. $\beta = 1$), the value taken by the ‘mean’ (i.e. emissivity averaged) ionization parameter (\bar{U}), as well as the line ratios, does not change with increasing intensity of the ionizing radiation. The authors did not explore in detail how such a stratification might come about. The hydro-static solution presented above, however, shows that radiation pressure, if important ($U \gtrsim 0.2$), can induce such a gradient.

Let us adopt the same definition of the ‘mean’ ionization parameter as BR90 :

$$\bar{U} = \frac{q_0}{\bar{n}c}, \quad (A.12)$$

where \bar{n} is the mean density, weighted by the local emissivity of the gas (which we take to be proportional to n^2) :

$$\bar{n} = \frac{\int_{x_S}^{\infty} [n(x)]^2 n(x) dx}{\int_{x_S}^{\infty} [n(x)]^2 dx}. \quad (A.13)$$

where the inner limit of integration is x_S , the position of the ‘Strömgren boundary’ which is assumed to be abrupt. x_S is given by :

$$x_S = L \left[\frac{2\beta - 1}{n_0^2 \alpha_B L} S_0 + 1 \right]^{-1/(2\beta-1)}, \quad (A.14)$$

For the case that interests us ($\beta = 1$), BR90 found that the mean ionization parameter \bar{U} is simply given by :

$$\bar{U} = \frac{2\alpha_B}{c} n_0 L \approx 1.7 \times 10^{-23} n_0 L \left(\frac{T}{10^4 K} \right)^{-0.83}, \quad (\text{A.15})$$

and is therefore independent of the ionizing flux q_0 and depends only on the normalization constant $n_0 L$. BR90 found that the line ratios also become independent of the strength of the source (see their Fig. 2) except for the density sensitive lines which become collisionally suppressed as \bar{n} increases linearly with q_0 . As shown in Fig. 3 of Sect. 2.5, we obtain a similar result when the gradient results from radiation pressure.

Constant \bar{U} is obtained only in the case of a strong density gradient. BR90 showed that this condition requires $L \ll D_S^0$, where $D_S^0 = q_0 / (n_0^2 \alpha_B)$ is the Strömgen distance at which hydrogen would become neutral in the slab if it were of constant density $n(x) = n_0$ throughout (i.e. isochoric). We rewrite this condition (which applies only to the ‘built-in’ density stratification with $\beta = 1$ of BR90) in terms of q_0 or $U_0 = \frac{q_0}{n_0 c}$ as follows :

$$\frac{q_0}{n_0^2 \alpha_B L} = \frac{U_0 c}{\alpha_B n_0 L} = \chi \gg 1, \quad (\text{A.16})$$

In eq. 15, the normalization constant $n_0 L$ is a free parameter. To the extent that the above condition is satisfied, clouds of similar $n_0 L$ distributed at various r_i around a point-like ionizing source will have \bar{U} independent of the distance from the source (see BR90 for a discussion of the limitations of this property). For line ratios, the situation is more complex due to the process of collisional de-excitation which introduces a dependence of the emissivity on the critical density. Only in the low density regime are line ratios of all clouds of similar $n_0 L$ strictly constant, provided that $\chi \gg 1$ and the species of interest are fully contained within the ionization structure of the slab (between $x = L$ and $x = x_S$).

A.3. Implementation of radiation pressure in MAPPINGS IC

The treatment presented is a numerical expression of Sect. A.1 generalized to take into account the opacity of heavier elements. Since in a photoionization code the integration of the transfer equations proceeds from the irradiated face inward, let us introduce the spatial coordinate $y = L - x$. The code MAPPINGS IC divides the photoionized slab into N small layers ($N \sim 10^2$) of geometrical depth δy_i . Starting at $y = 0$, the code sequentially solves for the temperature and ionization balance at each of the boundaries i , that is at each $y_i = \sum_{j=0}^i \delta y_j$ (starting with $\delta y_0 = 0$). The gas densities n_i are derived from the equation of state, that is from the local gas pressure, P_{gas}^i . The gas pressure at boundary i must balance the cumulative pressure exerted by the outer gas layers $j < i$ as well as by the volume force exerted within δy_i by absorption of ionizing radiation. We therefore have :

$$P_{gas}^i = P_{gas}^{i-1} + (F_{rad}^{i-1} - F_c^{i-1}) \delta y_i, \quad (\text{A.17})$$

where F_{rad}^{i-1} is the volume force evaluated at y_{i-1} due to absorption of the impinging radiation and F_c^{i-1} a term representing the inertial and gravitational forces (see below). We have :

$$F_{rad}^i = \sum_{m=1} \sum_{k=0} n_i(X_m^{+k}) \int_{\nu_m^k}^{\infty} \frac{\varphi_\nu e^{-\tau_\nu^i}}{h\nu} \frac{h\nu}{c} a_\nu(X_m^{+k}) d\nu, \quad (\text{A.18})$$

where $n_i(X_m^{+k})$ is the number density of ion $+k$ of atomic species m within layer δy_i , $a_\nu(X_m^{+k})$ the corresponding photoionization cross section with threshold ν_m^k and τ_ν^i the cumulative opacity up to y_i :

$$\tau_\nu^i = \sum_{j=1}^i \sum_{m=1} \sum_{k=0} n_j(X_m^{+k}) a_\nu(X_m^{+k}) \delta y_j, \quad (\text{A.19})$$

The summations in A.18 and A.19 are carried over all ions of significant abundance and can be generalized to include continuous opacity due to dust extinction.

The implementation of bulk acceleration and gravity will be the subject of a subsequent paper. For completeness, let us define F_c^i as :

$$F_c^i = (g_{bh,*} + a_{cl}) \rho_i = a'_e \rho_i, \quad (\text{A.20})$$

where ρ_i is the density in g cm^{-3} , $g_{bh,*} = GM_{bh,*}/r^2$ the acceleration due to the nuclear blackhole and/or stellar masses and a_{cl} the bulk acceleration of the whole cloud (cf. Mathews 1986). Only the effective acceleration $a'_e = g_{bh,*} + a_{cl}$ needs to be defined in our calculations. For future work, we define this input parameter as Ψ_0 , the ratio of effective acceleration to radiative acceleration at the irradiated face : $\Psi_0 = a'_e \rho_0 / F_{rad}^0 = F_c^0 / F_{rad}^0$. In this work we have set $\Psi_0 = 0$ (i.e. $F_c^i = 0$). This corresponds to the situation in which the photoionized clouds are pushing (without acceleration) against a hot and tenuous medium with the compression being counterbalanced by the drag force. Adopting a formalism similar to Mathews (1986), the relative pressure difference between the irradiated face and the back of the slab, $\delta\Pi$, is :

$$\delta\Pi = (P_{gas}^{back} - P_{gas}^0) / \text{MIN}(P_{gas}^{back}, P_{gas}^0), \quad (\text{A.21})$$

It represents the ratio of drag pressure to external pressure (i.e. the dynamical pressure of the ‘pushing’ clouds whenever $\delta\Pi > 0$). For the MB slab with $U_0 = 0.5$ discussed in Sect. 2, we obtain $\delta\Pi = 1.6$. In the simple case $\Psi_0 = 0$, the increase in pressure across the slab due to absorption of radiation is given by :

$$P_{rad}^{abs} = \sum_{i=1}^N F_{rad}^{i-1} \delta y_i = \delta\Pi P_{gas}^0, \quad (\text{A.22})$$

A significant gradient in density or gas pressure will only occur if the available radiation pressure is sufficiently high. Therefore, in the case of stratification due to radiation pressure, the condition for constant \bar{U} discussed in Sect. 2.3 (with $\Psi_0 = 0$) can be expressed as follows :

$$\frac{P_{rad}^{abs}}{P_{gas}^0} = \delta\Pi > 1, \quad (A.23)$$

where P_{gas}^0 is the gas pressure at the irradiated surface. [This condition differs from eq A.14 above which concerned only the ‘built-in’ density stratification discussed in BR90.]

The above density prescription remains an idealized way of considering radiation pressure and is not intended to describe the full complexity of photoionized regions. Clouds submitted to significant radiation pressure are particularly prone to derimming through the establishment of a lateral flow as shown by Mathews (1986). Mathews & Veilleux (1989) have reviewed the problem of cloud stability under conditions appropriate to the NLR.

References

- Acosta-Pulido, J. A., Vila-Vilaro, B., Perez-Fournon, I., Wilson, A. S., Tsvetanov, Z. I., 1996, *ApJ* 464, 177
- Anders, E., Grevesse, N. 1989, *Geochim. Cosmochim. Acta* 53, 197
- Binette, L. 1984, *A&A* 143, 334
- Binette, L., Raga, A. C. 1990, *AJ* 100, 1046 (BR90)
- Binette L., Wilson, A. S., Storchi-Bergmann, T. 1996, *A&A* 312, 365 (Paper I)
- Contini, M., Viegas-Aldrovandi, S. M. 1989, *ApJ* 343, 78
- Davidson, K. 1972, *ApJ* 171, 213
- Dopita, M. A., Sutherland, R. S. 1996, *ApJS* 102, 161
- Ferland, G. J., Osterbrock D. E. 1986, *ApJ* 300, 658
- Ferruit, P., Binette, L., Sutherland, R. S., Pécontal, E. 1997, *A&A* 322, 73
- Komossa, S., Fink, H. 1997a, *A&A* 322, 719
- Komossa, S., Fink, H. 1997b, *A&A*, in press (MPE preprint #387)
- Komossa, S., Schulz, H. 1997, *A&A* 323, 31
- Korista, K. T., Ferland, G. J. 1989, *ApJ* 343, 678
- Krolik, J. H., McKee, C., Tarter, C. B. 1981, *ApJ* 249, 422
- Mathews, W. G. 1986, *ApJ* 305, 187
- Mathews, W. G., Ferland, G. J. 1987, *ApJ* 323, 456
- Mathews, W. G., Veilleux, S. 1989, *ApJ* 336, 93
- Mohan, M., Hibbert, A., Kingston, A. E., *ApJ* 434, 389
- Morganti, R., Robinson, A., Fosbury, R. A. E., di Serego Alighieri, S., Tadhunter, C. N., Malin D. F., 1991, *MNRAS* 249, 91
- Moore, D., Cohen, R. D., 1994, *ApJ* 433, 602
- Moore, D., Cohen, R. D., 1996, *ApJ* 470, 301
- Moorwood, A. F. M., Lutz, D., Oliva, E., Marconi, A., Netzer, H., Genzel, R., Sturm, E., de Graauw, T. 1996, *A&A* 315, L109 (Mo96)
- Nazarova, L. S., O’Brien, P. T., Ward, M. J., 1997, *A&A* in press
- Oliva, E., in proc. of Emission lines in active galactic nuclei: new methods and techniques, *IAU Coll. 159, ASP Conf series* 113, p.288
- Oliva, E., Salvati, M., Moorwood, A. F. M., Marconi, A. 1994, *A&A* 288, 457 (OSMM)
- Osterbrock, D., 1989, in *Astrophysics of gaseous nebulae and active galactic nuclei*, University Science Books: Mill Valley
- Pelan, J. C., Berrington, K. A. 1995, *A&AS* 110, 209
- Penston, M. V., Fosbury, R. A. E., Boksenberg, A., Ward, M. J., Wilson, A. S. 1994, *MNRAS* 208, 347
- Robinson, A. et al. 1994, *A&A* 291, 351
- Rodriguez-Ardilla, A., Pastoriza, M. G., Maza, J., 1997, *ApJ* in press
- Stasińska, G. 1984, *A&A* 135, 341
- Storchi-Bergmann, T., Wilson, A. S., Mulchaey J.S., Binette L. 1996, *A&A* 312, 357
- Tadhunter, C. N., Robinson, A., Morganti, R., 1989, in: *ESO Workshop on Extranuclear Activity in Galaxies*, eds Meurs, E. J. A., Fosbury, R. A. E., *ESO Conf. and Workshop Proc. No. 32*, Garching, p. 293
- Viegas, S. M., Gruenwald, R. B. 1988, *ApJ* 324, 683
- Viegas, S. M., Prieto, A. 1992, *MNRAS* 258, 483
- Villar-Martín, M., Binette, L. 1996, *A&A* 309, 97
- Wilson, A. S., Binette, L., Storchi-Bergmann, T. 1997, *ApJL* 482, L131